



**HAL**  
open science

## Effect of shell thickness of gold-silica core-shell nanospheres embedded in an organic buffer matrix for plasmonic solar cells

Kekeli N’Konou, Véronique Many, Carmen Ruiz, Mona Tréguer-Delapierre, Philippe Torchio

### ► To cite this version:

Kekeli N’Konou, Véronique Many, Carmen Ruiz, Mona Tréguer-Delapierre, Philippe Torchio. Effect of shell thickness of gold-silica core-shell nanospheres embedded in an organic buffer matrix for plasmonic solar cells. *Journal of Applied Physics*, 2018, 123 (6), pp.063102. 10.1063/1.5013329 . hal-01719727

**HAL Id: hal-01719727**

**<https://hal.science/hal-01719727v1>**

Submitted on 23 Mar 2022

**HAL** is a multi-disciplinary open access archive for the deposit and dissemination of scientific research documents, whether they are published or not. The documents may come from teaching and research institutions in France or abroad, or from public or private research centers.

L’archive ouverte pluridisciplinaire **HAL**, est destinée au dépôt et à la diffusion de documents scientifiques de niveau recherche, publiés ou non, émanant des établissements d’enseignement et de recherche français ou étrangers, des laboratoires publics ou privés.

## Effect of shell thickness of gold-silica core-shell nanospheres embedded in an organic buffer matrix for plasmonic solar cells

Kekeli N'Konou, Véronique Many, Carmen M. Ruiz, Mona Treguer-Delapierre, and Philippe Torchio

Citation: *Journal of Applied Physics* **123**, 063102 (2018); doi: 10.1063/1.5013329

View online: <https://doi.org/10.1063/1.5013329>

View Table of Contents: <http://aip.scitation.org/toc/jap/123/6>

Published by the *American Institute of Physics*

---

### Articles you may be interested in

[Optical properties of electrically connected plasmonic nanoantenna dimer arrays](#)

*Journal of Applied Physics* **123**, 063101 (2018); 10.1063/1.5008511

[Theory of electromagnetic wave propagation in ferromagnetic Rashba conductor](#)

*Journal of Applied Physics* **123**, 063902 (2018); 10.1063/1.5011130

[Charge transport and electron-hole asymmetry in low-mobility graphene/hexagonal boron nitride heterostructures](#)

*Journal of Applied Physics* **123**, 064303 (2018); 10.1063/1.5009742

[Ion energy distributions in highly transient EUV induced plasma in hydrogen](#)

*Journal of Applied Physics* **123**, 063301 (2018); 10.1063/1.5017303

[An analytic investigation for the edge effect on mechanical properties of graphene nanoribbons](#)

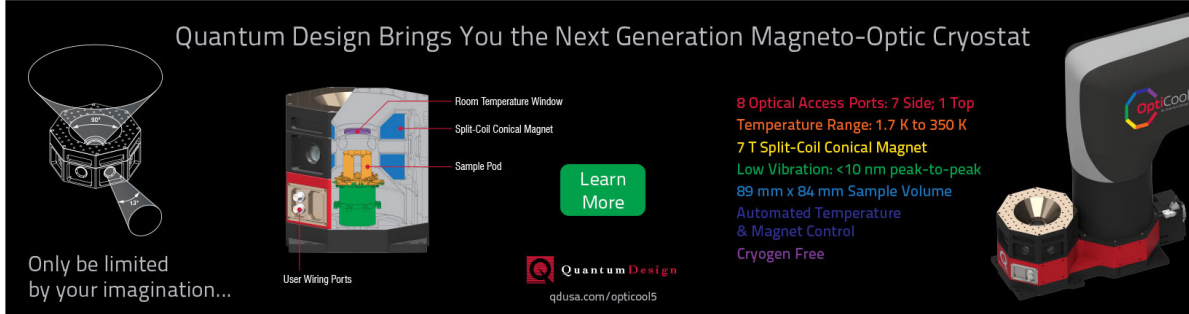
*Journal of Applied Physics* **123**, 064301 (2018); 10.1063/1.5012562

[Enhanced graphene nonlinear response through geometrical plasmon focusing](#)

*Applied Physics Letters* **112**, 061107 (2018); 10.1063/1.5017120

---

Quantum Design Brings You the Next Generation Magneto-Optic Cryostat



Only be limited by your imagination...

Room Temperature Window  
Split-Coil Conical Magnet  
Sample Pod  
User Wiring Ports

Learn More

Quantum Design  
qdusa.com/opticool5

8 Optical Access Ports: 7 Side; 1 Top  
Temperature Range: 1.7 K to 350 K  
7 T Split-Coil Conical Magnet  
Low Vibration: <10 nm peak-to-peak  
89 mm x 84 mm Sample Volume  
Automated Temperature & Magnet Control  
Cryogen Free

OptiCool

## Effect of shell thickness of gold-silica core-shell nanospheres embedded in an organic buffer matrix for plasmonic solar cells

Kekeli N'Konou,<sup>1</sup> Véronique Many,<sup>2</sup> Carmen M. Ruiz,<sup>1</sup> Mona Treguer-Delapierre,<sup>2</sup> and Philippe Torchio<sup>1,a)</sup>

<sup>1</sup>Aix-Marseille University, Institut Matériaux Microélectronique Nanosciences de Provence-IM2NP, CNRS-UMR 7334, Domaine Universitaire de Saint-Jérôme, Service 231, 13397 Marseille Cedex 20, France

<sup>2</sup>University of Bordeaux, Institut de Chimie de la Matière Condensée de Bordeaux, ICMCB, CNRS-UPR 9048, 33600 Pessac, France

(Received 13 November 2017; accepted 21 January 2018; published online 8 February 2018)

The integration of metal nanoparticles in an organic buffer matrix for plasmonic organic solar cells (OSCs) has been explored as a route for improving the photovoltaic performance, with localized electromagnetic field enhancement around nanoparticles. We investigate the optical behavior of gold-silica core-shell nanospheres (Au@SiO<sub>2</sub> NSs) with different shell thicknesses integrated into a 30 nm-thick poly(3,4-ethylenedioxythiophene)-poly(styrenesulfonate) layer which is traditionally used as a buffer layer in OSCs. The morphology and size of the chemically synthesized Au@SiO<sub>2</sub> NSs are determined by TEM, indicating that the average diameter of the Au core is about 50 nm, while the thickness of the dielectric shell can be adjusted to around 5 or 10 nm. The effect of Au@SiO<sub>2</sub> NSs on the surrounding electromagnetic field in such a heterogeneous matrix and subsequent multilayers is examined using a numerical simulation based on a 3D-FDTD method. Furthermore, a broadband absorption enhancement in the films, which can be primarily attributed to far-field scattering and also to the localized surface plasmon resonance around the wavelength of 530 nm, is observed in the simulated and measured absorption spectra. The analysis of the electromagnetic field between NSs and the active layer using Raman spectroscopy is also presented. The Raman spectra confirm that a plasmon effect occurs and induces a strong field enhancement; this does not change the Raman peak position but increases its signal intensity depending on the silica shell's thickness. As a result, plasmonic devices including Au@SiO<sub>2</sub> NSs with a 5 nm-shell thickness present the best optical behavior compared to bare NSs or 10 nm-thick shell Au@SiO<sub>2</sub> NSs.

Published by AIP Publishing. <https://doi.org/10.1063/1.5013329>

### I. INTRODUCTION

Due to low-production-cost, mechanical flexibility, solution processability, potential for large-area manufacturing, and lightweight, organic solar cells (OSCs) have been revealed as an alternative solution for solar cell devices.<sup>1–3</sup> The power conversion efficiency (PCE) of OSCs is showing significant progress every year, and PCE over 13% has been obtained by Zhao *et al.*<sup>4</sup> However, their PCE, still relatively low compared to inorganic solar cells, reduces their further application. This is due to short exciton diffusion lengths and low charge carrier mobilities, limiting the photoactive layer thickness.<sup>5,6</sup>

Therefore, one of the challenges in OSC absorption enhancement is to find the compromise between the efficient photogenerated carrier collection, as in thin active layers, and light absorption, which requires a thick active layer. Many light-trapping strategies such as the introduction of a surface plasmon effect, induced by either metallic nanostructures<sup>7,8</sup> or photonic crystals,<sup>9,10</sup> are widely studied for improving light absorption in OSCs. The incorporation of metallic nanoparticles (MNPs) inside the buffer layer or the active layer of OSCs has been explored as one of the promising routes to enhance the light absorption with near-field localized surface plasmonic resonance (LSPR) or far-field light scattering from MNPs. These

proposed mechanisms could improve the light absorption and increase the optical path length.<sup>11–15</sup> Nevertheless, the use of bare MNPs in contact with the active layer in thin-film OSC devices involves the increase in the charge recombination and exciton quenching, leading to efficiency losses.<sup>16,17</sup> Thus, these electrical losses offset the optical enhancement produced by the MNPs.<sup>18</sup> Moreover, the possible migrations or segregations of the MNPs in the undesired areas of a cell could lead to shunt currents, which are also detrimental to the electrical properties of photovoltaic devices. To eliminate these issues, the MNPs can be coated with a dielectric shell. The position of core-shell nanoparticles (NPs) inside the OSC devices should improve light scattering and absorption through electromagnetic field distribution. To maximize hole collection and reduce exciton quenching, some research groups incorporated the MNPs or core-shell MNPs at the interface of Indium Tin Oxide (ITO) and poly(3,4-ethylenedioxythiophene):polystyrene sulfonic acid (PEDOT:PSS)<sup>19</sup> or in the PEDOT:PSS layer.<sup>20,21</sup> Choi *et al.*<sup>22</sup> integrated silica-coated silver nanoparticles between PEDOT:PSS and the active layer in order to prevent possible NP aggregations inside the active layer or disturb its morphology. Their results revealed a remarkable enhancement of PCE. The latter is attributed to the light scattering and absorption via strong near-field distribution inside the active layer, the enlarged contact area between the buffer and the active layer, and the enhancement of the buffer layer conductivity.

<sup>a)</sup>philippe.torchio@univ-amu.fr

Hao *et al.*<sup>23</sup> demonstrated that the use of silica-coated silver nanoparticles in the buffer layer improves the performance of OSCs with a relative gain of 22% in PCE. The authors demonstrated that the integration of spherical core-shell NPs inside the buffer layer, including some large NPs that penetrate partly into the active layer, generated an increase in PCE. Based on these results, a large metallic core diameter will be synthesized with the ability to protrude partially inside the active layer for increasing light-harvesting capacity via light scattering and the LSPR effect inside the active layer. The dielectric shell thickness is a key design parameter of metallic-dielectric core-shell NPs. Few articles addressed the impact of the silica shell thickness surrounding MNPs to increase the OSC performance except those originating from gold-silica nanorods embedded between the PEDOT:PSS layer and the thieno[3,4-b]thiophene/benzodithiophene PTB7:PC<sub>71</sub>BM active layer interface<sup>24</sup> or inside the 7,7'-(4,4-bis(2-ethylhexyl)-4H-silolo[3,2-b:4,5-b']-dithiophene-2,6-diyl)bis(6-fluoro-4-(5'-hexyl-[2,2'-bithiophen]-5-yl)benzo[c][1,2,5]thiadiazole) (p-DTS(FBTTh<sub>2</sub>)<sub>2</sub>):PC<sub>71</sub>BM active layer.<sup>25</sup> In this regard, the results converged and demonstrated that an ultra-thin silica shell enhanced efficiently the OSC performance, which was consistent with our numerical results.<sup>26</sup> In disagreement, Chen *et al.*,<sup>27</sup> by following their finite-difference time-domain method (FDTD) simulations, revealed that the optimum thickness for the SiO<sub>2</sub> shell is found to be 50 nm. This result is not consistent with the experimental studies addressed on the effect of the silica shell thickness on OSC performance enhancement. In addition, the authors used large Au@SiO<sub>2</sub> NPs (Au NPs with an approximate size of 70 nm coated by an ~50 nm-thick SiO<sub>2</sub> shell) that penetrated all organic layers and partially embedded in the Al cathode layer. On the other hand, our recent numerical studies<sup>26</sup> predicted that if the dielectric shell is too thick, the localized electromagnetic field enhancement effect around the NPs embedded in the active layer would be greatly diminished. To clear up any doubts about the theoretical results, an experimental study on the silica shell thickness is needed to confirm or rule out our numerical results<sup>26</sup> or other experimental results presented in the literature.<sup>24,25</sup>

The goal of this paper is to treat Au nanospheres with an approximate size of 50 nm coated with an ~5 and 10 nm-thick SiO<sub>2</sub> shell (Au@SiO<sub>2</sub> NSs) embedded within the PEDOT:PSS buffer layer and partly penetrating inside the active layer. The nanospheres are chosen unlike other shapes of NPs to be closer to our numerical structure design previously studied in Ref. 26. Kelly *et al.* demonstrated that the MNP shape affects their optical properties, thereby showing that the optical behavior of nanorods MNPs differ from that of nanospheres.<sup>28</sup> Gold and poly(3-hexylthiophene-2,5-diyl)-[6,6]-phenyl-C<sub>61</sub>-butyric acid methyl ester (P3HT:PCBM) are chosen as the core material of core-shell NSs and the active layer, respectively, in order to compare the expected experimental results with the ones existing in the literature.

This work deals about the integration of gold-silica core-shell nanospheres with different shell thicknesses in the PEDOT:PSS layer which is traditionally used as an anodic buffer layer in organic solar cells. The objective is to enhance the absorption inside the adjacent photoactive layer without

enlarging its thickness by a light-trapping strategy based on the surface plasmon effect. To the best of our knowledge, no correlated numerical to experimental study has been focused on the impact on the optical behavior of the shell thickness in gold-silica core-shell nanospheres embedded in an organic buffer matrix. As cited before, only a few results have been reported, either theoretical or experimental on nanospheres or derived from other morphologies (such nanorods). In addition, no study correlated with the plasmonic effects of metallic-dielectric core-shell NPs embedded in organic solar cells has been yet reported using Raman spectroscopy. In the literature, some authors have already used Raman spectroscopy to analyze the electromagnetic field between bare MNPs and polymers<sup>29</sup> and the structural changes of the conjugated polymers near the bare MNPs<sup>30</sup> by the relative intensity and the peak position.

In this paper, we experimentally and theoretically report the effects of the (0 nm, 5 nm, and 10 nm) silica shell thicknesses of gold-silica core-shell nanospheres (Au@SiO<sub>2</sub> NSs) on the optical behavior of an organic buffer matrix made of the poly(3,4-ethylenedioxythiophene)-poly(styrenesulfonate) (PEDOT:PSS) layer. Chemical synthesis is described for the preparation of Au NSs, while the absorption properties of Au NSs coated with different silica shell thicknesses are investigated via spectrophotometry. Furthermore, the influence of such Au@SiO<sub>2</sub> NSs on the morphology of the PEDOT:PSS layer and on the electromagnetic field distribution around Au@SiO<sub>2</sub> NSs is obtained by using AFM and numerical simulation based on a Finite Difference Time Domain (FDTD) method, respectively.

## II. EXPERIMENTAL

### A. Materials

KAuCl<sub>4</sub>, trisodium citrate, cetyltrimethylammonium bromide (CTAB), Gold(III) chloride trihydrate 5 H<sub>2</sub>O, Ascorbic acid, cetyltrimethylammonium bromide (CTAB), Orthosilicate de tétraéthyle (TEOS), ammonia, and m(PEG)-SH (O-[2-(3 Mercaptopropionylamino) ethyl]-O-methylpolyethylene glycol)) are obtained from Sigma Aldrich.

### B. Preparation of Au@SiO<sub>2</sub> core/shell NSs

#### 1. Synthesis of Au NSs

Gold seeds of 12 nm are synthesized according to the method described by Wang *et al.*<sup>31</sup> Subsequently, the 12 nm gold nanoparticles are regrown to 50 nm nanospheres (Au NSs) by the seeded growth method.<sup>32</sup> Typically, in a 1 l round bottom flask, 15 mM CTAB is dissolved in water and stirred at 35 °C and 0.5 mM of H<sub>2</sub>O are added to the solution, followed by the addition of 1 mM of ascorbic acid and 2 ml of gold seeds. After 1 h of reaction, the gold NSs are centrifuged and redispersed in 1 ml of water and purified by Jana method<sup>33</sup> to remove the remaining nanorods in the colloidal suspension.

#### 2. Synthesis of Au@SiO<sub>2</sub> NSs

The encapsulation of the gold nanoparticles with a thin layer of silica is performed following a procedure described

by Pastoriza-Santos *et al.*<sup>34</sup> Gold nanoparticles of 50 nm diameter are chemically modified by O-[2-(3-mercaptopropionylamino)ethyl]-O-methylpoly-ethylene glycol (PEG-SH). Briefly, an amount of PEG-SH corresponding to 4 functions/nm<sup>2</sup>, previously redispersed in 500  $\mu$ l of water, is added drop by drop to the colloidal suspension and stirred vigorously for 2 h. The pegylated gold nanoparticles are then centrifuged and redispersed in 1 ml of water. A silica shell is grown on the Au NS surface by a conventional Stöber method.<sup>35</sup> In brief, 0.5 mM of gold nanoparticles are redispersed in 10.5 M of water and ethanol (1:4). 0.2 M of ammonia are added to the mixture. Finally, 0.8 mM and 0.4 mM of TEOS are added drop by drop to the colloidal solution to get 5 nm and 10 nm of silica shells, respectively. The solution is stirred for 6 h.

### C. Preparation of the multilayer films

Initially, the ITO-coated glass substrates (Lumtec<sup>©</sup>) are cleaned successively for 10 min by ultrasonic treatment in detergent, deionized water, acetone, and ethanol and then blown dry using N<sub>2</sub> gas just before deposition of PEDOT:PSS (CLEVIOS PVP Al 4083). The PEDOT:PSS solution is diluted with deionized water in 1:1 volume ratio in order to reduce its acidity. The Au nanospheres with silica shell thicknesses of 0 nm, 5 nm, and 10 nm solutions with the same concentration (optimized doping concentration of 4.3.10<sup>14</sup> particles/l) will be named as Au NSs, Au@SiO<sub>2</sub> (5 nm) NSs, and Au@SiO<sub>2</sub> (10 nm) NSs, respectively. Each mixed solution is prepared by adding 400  $\mu$ l of Au NS, Au@SiO<sub>2</sub> (5 nm) NSs, or Au@SiO<sub>2</sub> (10 nm) NS solution to 1 ml of the previous PEDOT:PSS solution. Consequently, the mixed solution is sonicated for 20 min to obtain a uniform dispersion of the NSs into PEDOT:PSS aqueous solution. Then, it is filtered using a polyvinylidene fluoride (PVDF) filter with a pore size of 0.45  $\mu$ m in order to remove the main clusters. 300  $\mu$ l of each mixed solution is spun at 3500 rpm for 60 s onto the pre-treated ITO glass substrates to form thin films of approximately 35  $\pm$  5 nm in thickness. Afterwards, the PEDOT:PSS-coated samples are deposited on a hot plate and annealed at 120 °C for 10 min to remove any residual water. Finally, the P3HT:PC<sub>60</sub>BM solution is prepared by dissolving the P3HT (10 mg) and PC<sub>60</sub>BM (10 mg) blend in 1 ml of chlorobenzene. This solution is stirred for 24 h at 50 °C to promote complete dissolution. 40  $\mu$ l of P3HT:PC<sub>60</sub>BM blend solution is subsequently deposited by spin-coating at 4000 rpm for 60 s in a glove box on top of the PEDOT:PSS layer forming a thick layer of approximately 60 nm.

### D. Measurement techniques

The optical properties of ITO/PEDOT:PSS without and with Au@SiO<sub>2</sub> NSs with different silica shell thickness/P3HT:PC<sub>60</sub>BM multilayer samples are measured using a UV/Vis/near-IR spectrophotometer (Perkin Elmer Lambda 950). The absorption (A) is obtained from reflection (R) and transmission (T) by the equation:  $A = 1 - R - T$ . TEM images are obtained using a Hitachi H600 microscope operating at 75 kV and using a Hitachi H7650 operating at 120 kV. The surface morphology of the films is obtained by atomic force microscopy (CSI Nano-Observer AFM), while Raman spectra are

obtained using a Horiba Jobin-Yvon HR800 spectrometer with a laser excitation wavelength of 633 nm from a HeNe laser.

## III. RESULTS AND DISCUSSION

Figure 1 presents the TEM images of bare Au NSs and the coated particles as well as the absorbance spectral changes observed from silica deposition. The method adopted yields highly monodisperse spherical particles; polydispersity never exceeded 5%. The monodispersity is preserved after the encapsulation of the metallic particles by the glass shell of different thicknesses (5 and 10 nm). The silica shell insulates entirely and uniformly the surface of each Au NS. The UV-Vis absorption spectrum of Au NSs dispersed in deionized water presents a surface plasmon resonance peak around 530 nm. Considering that the absorption band matches with the range of the absorption spectrum of P3HT:PC<sub>60</sub>BM (whose bandgap is approximately 1.9 eV), it can be predicted that the incorporation of such Au NSs into OSCs could enhance light absorption in these devices through LSPR effects.

The possible influence of Au NSs and Au@SiO<sub>2</sub> NSs on the morphology of the composite PEDOT:PSS layer is investigated. The AFM images of PEDOT:PSS films without and with NSs are given in Fig. 2. The surface morphology changes can be attributed to the incorporation of NSs. As it can be seen, the integration of Au NSs and Au@SiO<sub>2</sub> NSs has a moderate influence on the Root-Mean-Square (RMS) roughness of the composite matrix buffer, which increases from 1.17 nm to 1.60 nm. It has also been demonstrated that increasing surface roughness can enhance the interface area between PEDOT:PSS and the active layer, which can promote a shortcut route for holes to move to the anode, allowing the hole collection to be enhanced.<sup>36</sup>

After coating previous samples with the P3HT:PCBM bulk heterojunction, their structure is composed as follows: glass/ITO/PEDOT:PSS/P3HT:PCBM (reference), glass/ITO/PEDOT:PSS with Au NSs/P3HT:PCBM and glass/ITO/PEDOT:PSS with Au@SiO<sub>2</sub> (5 or 10 nm) NSs/P3HT:PCBM [Fig. 3(a)]. These designs will be considered and named thereafter as OSCs, even if the metal cathode is missing. These multilayers are then optically characterized by spectrophotometry to investigate their optical behavior.

Figure 3(b) presents the experimental absorption spectra of the multilayer films without and with NSs. A broadband absorption enhancement is observed in the majority of the spectral range from 300 to 800 nm wavelength upon incorporation of NSs into the PEDOT:PSS buffer layer except in the [480–530] nm range. The highest absorption enhancement is obtained with Au@SiO<sub>2</sub> (5 nm) NSs embedded in the buffer layer, which indicates that a thin silica shell does not reduce the probable plasmonic absorption gain. Since Au@SiO<sub>2</sub> NSs have a larger diameter than non-coated NSs, the far-field scattering effect will be somewhat amplified. However, these absorption enhancements inside the P3HT:PCBM layer can be attributed not only to the far-field scattering effect but also to the LSPR effect.

The experimental UV-Vis absorption spectra of the thin films stacked on ITO/PEDOT:PSS are also compared with the FDTD simulation results. We perform optical simulations on design close to the experimental ones by using the FDTD

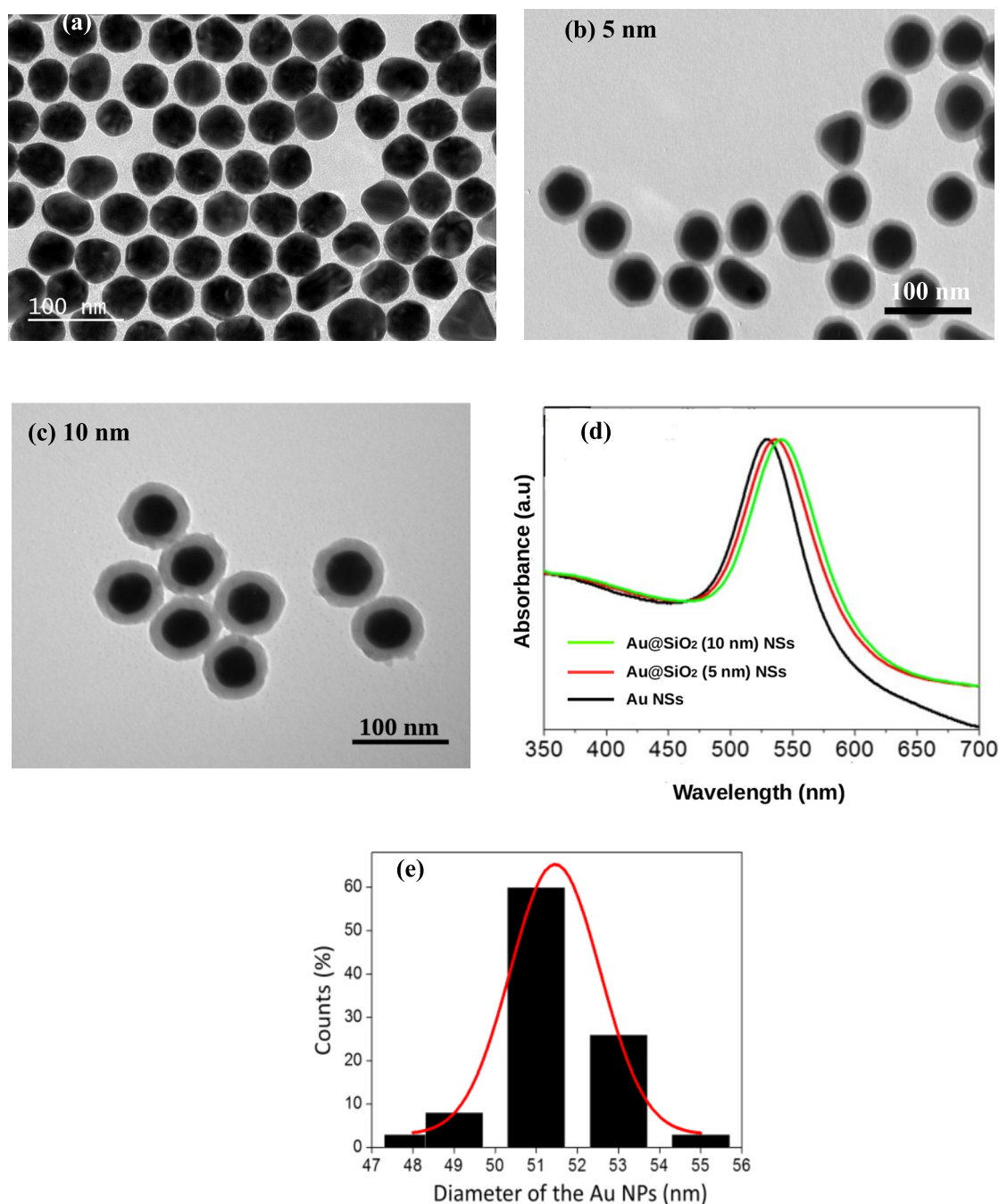


FIG. 1. TEM images of (a) bare Au NSs and Au@SiO<sub>2</sub> NSs with silica shell thicknesses of (b) 5 nm and (c) 10 nm; (d) UV-Vis spectra of Au NSs before and after silica encapsulation; and (e) Size distribution histogram of Au NSs.

method (by Lumerical FDTD Solutions<sup>©</sup> software). This method is based on solving Maxwell's equations and requires the optical constants of all materials as input data. The thicknesses of each layer from the stack: ITO/PEDOT:PSS/P3HT:PC<sub>60</sub>BM are 180/30/60 nm, respectively [the same design as samples of Fig. 3(a)], where Au core NSs have a 50 nm diameter with a 5 nm or 10 nm-thick SiO<sub>2</sub> shell. All calculations around metal/dielectric interfaces are performed with a 0.5 nm spatial mesh grid. The modeling details such as mesh sizes, boundaries, and optical constants for all the layers can be found in Ref. 26. The period (distance between NPs) is fixed at 320, 260, and 240 nm for Au NSs, Au@SiO<sub>2</sub> (5 nm) NSs, and Au@SiO<sub>2</sub> (10 nm) NSs, respectively. These period

values are determined from the average distance separating the NPs as observed in AFM images (Fig. 2).

The measured and simulated optical absorption spectra of the multilayers are presented in Figs. 3(b) and 3(c). The numerical results demonstrate an absorption enhancement in the 550–650 nm wavelength range when NSs are added to the films (by comparing with the reference sample). The enhancement band is broader when Au@SiO<sub>2</sub> (5 nm) NSs are embedded, with a beneficial red-shift of the secondary peak. The simulated absorption spectra [Fig. 3(c)] follow similar trends as the measured spectra [Fig. 3(b)]. However, the simulation data of the absorption are higher than those of the measurement data. These differences can be attributed to the optical

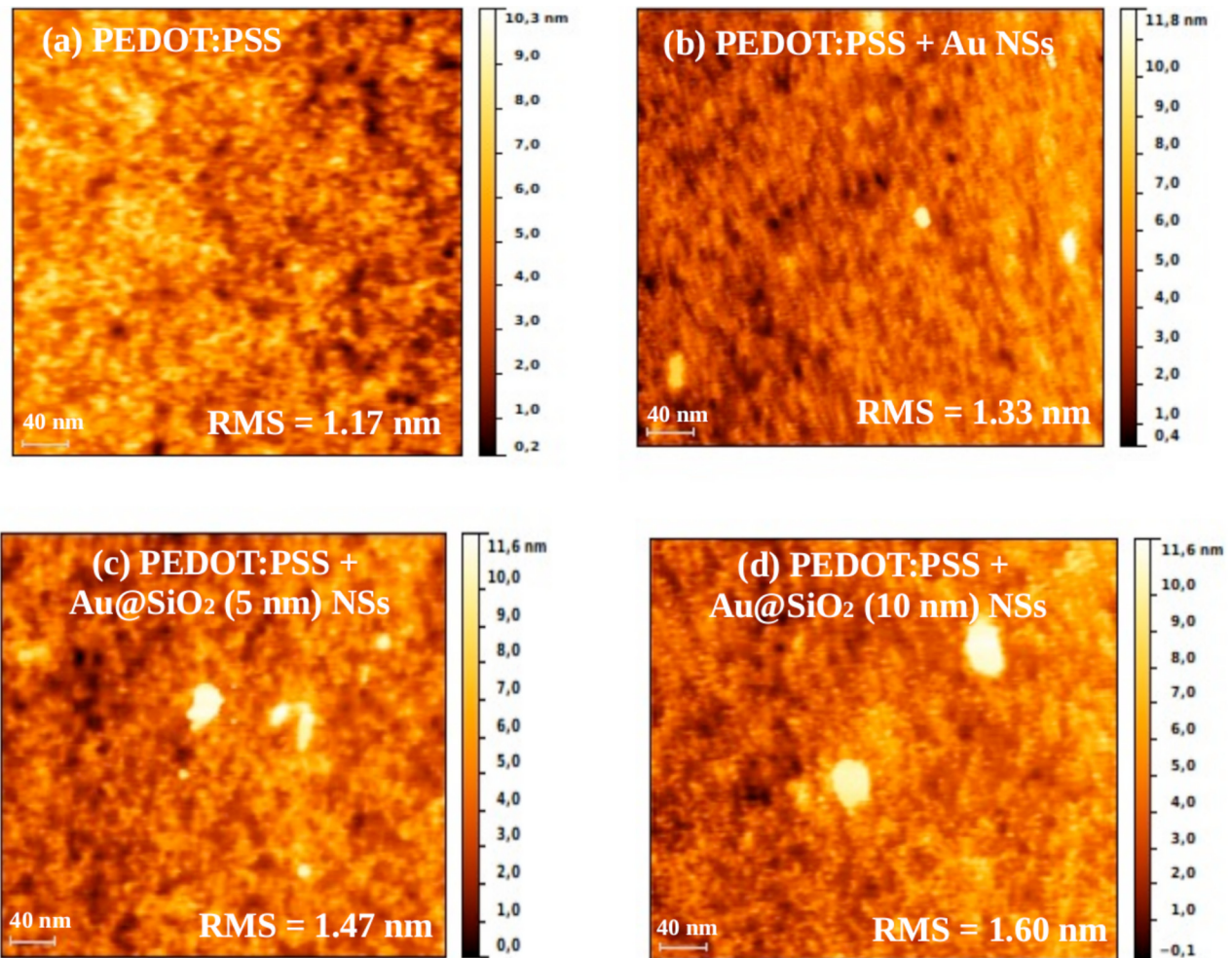


FIG. 2. AFM images of PEDOT:PSS films (a) without NSs, (b) with bare Au NSs, (c) with Au@SiO<sub>2</sub> (5 nm) NSs, and (d) with Au@SiO<sub>2</sub> (10 nm) NSs. Root Mean Square (RMS) surface roughness is calculated from data using Gwyddion software.

constants [ $n(\lambda)$  and  $k(\lambda)$ ] of the real materials, which can differ from those used in the modeling, and to the roughness of the films, which is not considered in the model (involving an underestimation of the external scattering for the simulation). Furthermore, the real NSs are not all spherical and are randomly distributed (i.e., not periodically), which can change or split the plasmon resonance band and enlarge the absorption enhancement band, as observed in Fig. 3(b).

In order to check that the LSP excited by the NSs can also improve light absorption in such multilayers, the distribution of the electromagnetic field around the Au@SiO<sub>2</sub> NSs is theoretically investigated. A plane wave in normal incidence illuminates the multilayers with a monochromatic excitation. The wavelengths of 530 nm and 633 nm are selected to map the electromagnetic field distribution because the wavelength of 530 nm represents the surface plasmon resonance peak of Au NS [as presented in Fig. 1(d)] and is placed in the maximum absorption band in the 400–660 nm range [as seen from Fig. 3(a)], while the wavelength of 633 nm is that of the HeNe laser excitation used for obtaining the Raman spectra.

The electromagnetic field maps are presented in Fig. 4. At  $\lambda = 530$  nm (top of the Fig. 4), the maximum of the electromagnetic field intensity around Au@SiO<sub>2</sub> (5 nm) NSs and Au@SiO<sub>2</sub> (10 nm) NSs is concentrated in the silica shell

and penetrates somewhat into the active layer, as well as for Au NSs. This indicates that the near-field effect contributes partially to the absorption enhancement in plasmonic samples at  $\lambda = 530$  nm. It can be noticed that the thick silica shell limits the extent of the localized enhanced electric field within the organic matrix. At  $\lambda = 633$  nm (bottom of the Fig. 4), the overall electromagnetic field intensity enhancement is around 3 times larger than that at  $\lambda = 530$  nm. At  $\lambda = 633$  nm, we also note that the near-field intensity around Au@SiO<sub>2</sub> (5 nm) NSs is more intense than that around Au@SiO<sub>2</sub> (10 nm) NSs inside the active layer [Figs. 4(b) and 4(c)], where the electric field intensity is mainly concentrated in the shell. This implies that integration of Au@SiO<sub>2</sub> (5 nm) NSs is able to contribute to a higher enhancement of the light absorption in the active layer.

We note that the exaltation of the electromagnetic field is extended around Au NSs in Fig. 4(a) (bottom) compared to Au@SiO<sub>2</sub> NSs, which might suggest that embedding Au NSs should lead to a better optical absorption enhancement than with Au@SiO<sub>2</sub> NSs; but this is not really confirmed by the previous results presented in Figs. 3(b) and 3(c). Consequently, the scattering of Ag@SiO<sub>2</sub> NPs should be a more valuable contributor to the light absorption enhancement than the LSPR effect. Other results from a follow-up research (Ref. 23) have also suggested that the embedded silica-coated silver

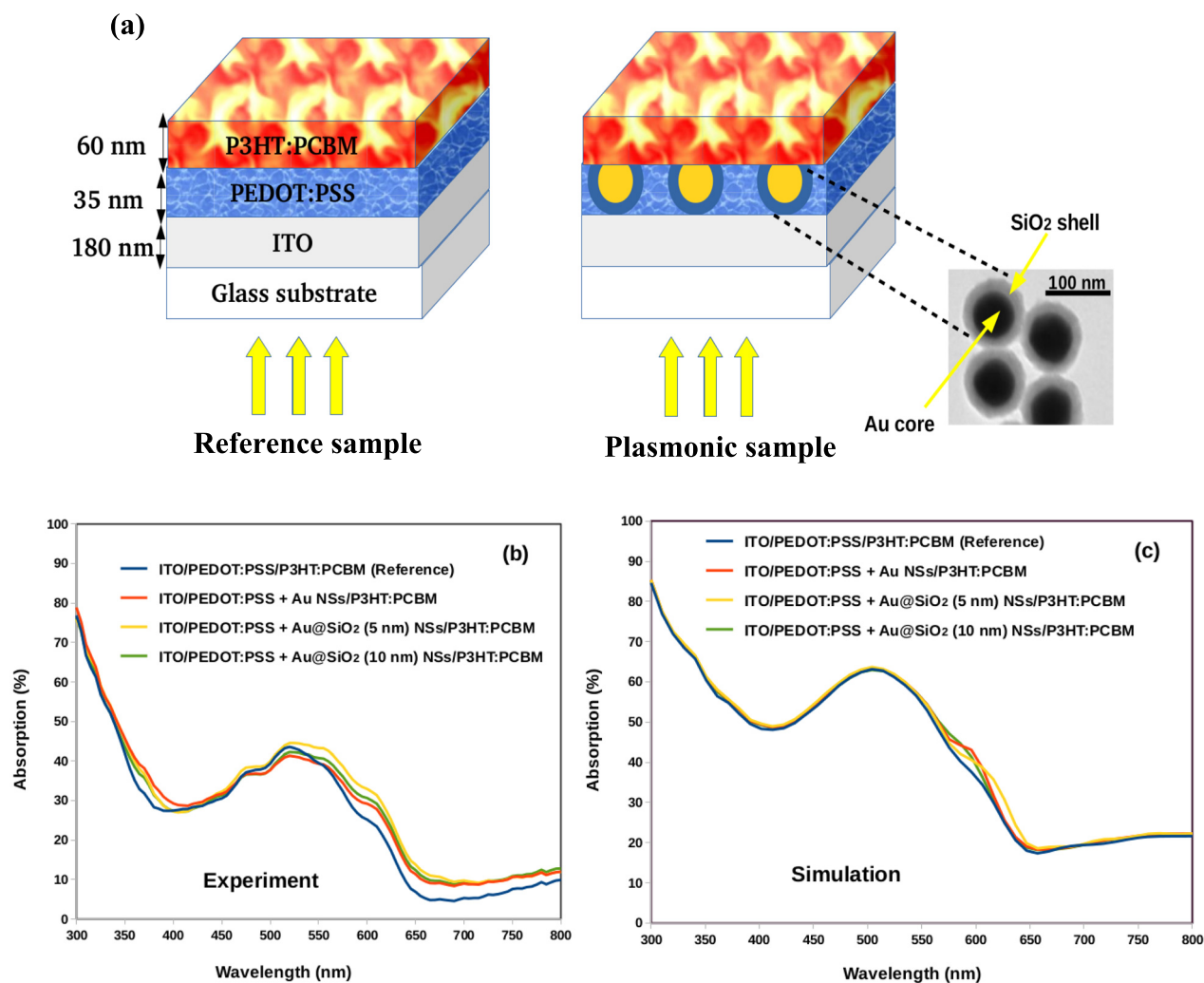


FIG. 3. (a) Device schematic of OSC without NSs blended into the PEDOT:PSS layer (left) and with Au@SiO<sub>2</sub> NSs blended into PEDOT:PSS solution (right). (b) Measured and (c) simulated UV-Vis absorption spectra of the thin films stacked on ITO/PEDOT:PSS.

nanoparticles (Ag@SiO<sub>2</sub> NPs) induce much stronger far-field scattering than bare Ag NPs.

Based on the experimental and numerical results, we demonstrate that a thick silica shell does not contribute to efficiently enhancing the optical absorption but that it is appropriate to coat MNPs with an ultrathin silica shell, in agreement in first instance with our numerical predictive results and those from the studies by Zhang *et al.*<sup>24</sup> and Xu *et al.*<sup>25</sup> The theoretical and experimental results demonstrate that if the silica shell is too thick (over 5 nm-thick), the electromagnetic field is primarily concentrated in the dielectric shell and should not contribute significantly to the absorption in the active layer. This is in contradiction with the Chen<sup>27</sup> findings, about an optimal silica shell thickness at 50 nm.

In general, the integration of MNPs also enables light to be scattered, which is especially useful in the active layer. The absorption enhancement is dependent on the metallic NP dimensions. When metallic NPs are incorporated into the organic solar cells, they can act as local electromagnetic field enhancers and/or light scatterers, and so, they can increase the optical path length without changing the actual thickness of the active layer. Some authors<sup>37–39</sup> reported that low

absorption in the metal nanoparticles is required when the MNPs are used for scattering light. Large particles give a larger scattering effect because the scattering cross-section  $C_{\text{Scat}}$  and absorption cross-section  $C_{\text{Abs}}$  are proportional to the diameter  $D$  of the particle [ $C_{\text{Scat}} \sim (D/2)^6$  and  $C_{\text{Abs}} \sim (D/2)^3$ ]. In other words, when the diameter increases, scattering from NPs is more enhanced than absorption and scattered light can be beneficially collected by the active layer.<sup>37,40</sup> Considering the size of our NSs, we suggest that Au@SiO<sub>2</sub> NSs induce higher light scattering within the active layer and contribute to light harvesting by plasmonic OSCs.

Raman spectroscopy is performed to check the impact of Au NSs with different shell thicknesses in the Raman response of the material under 633-nm excitation. This wavelength was previously demonstrated to present an electromagnetic field more intense in the photoactive material compared to  $\lambda = 530$  nm. Figure 5 presents the Raman spectra of a reference sample and plasmonic samples, while the inset shows the chemical structures of P3HT. The very low extinction coefficient of PCBM at this wavelength does not allow observing the Raman modes of this material. The characteristic Raman peaks of P3HT are found in the



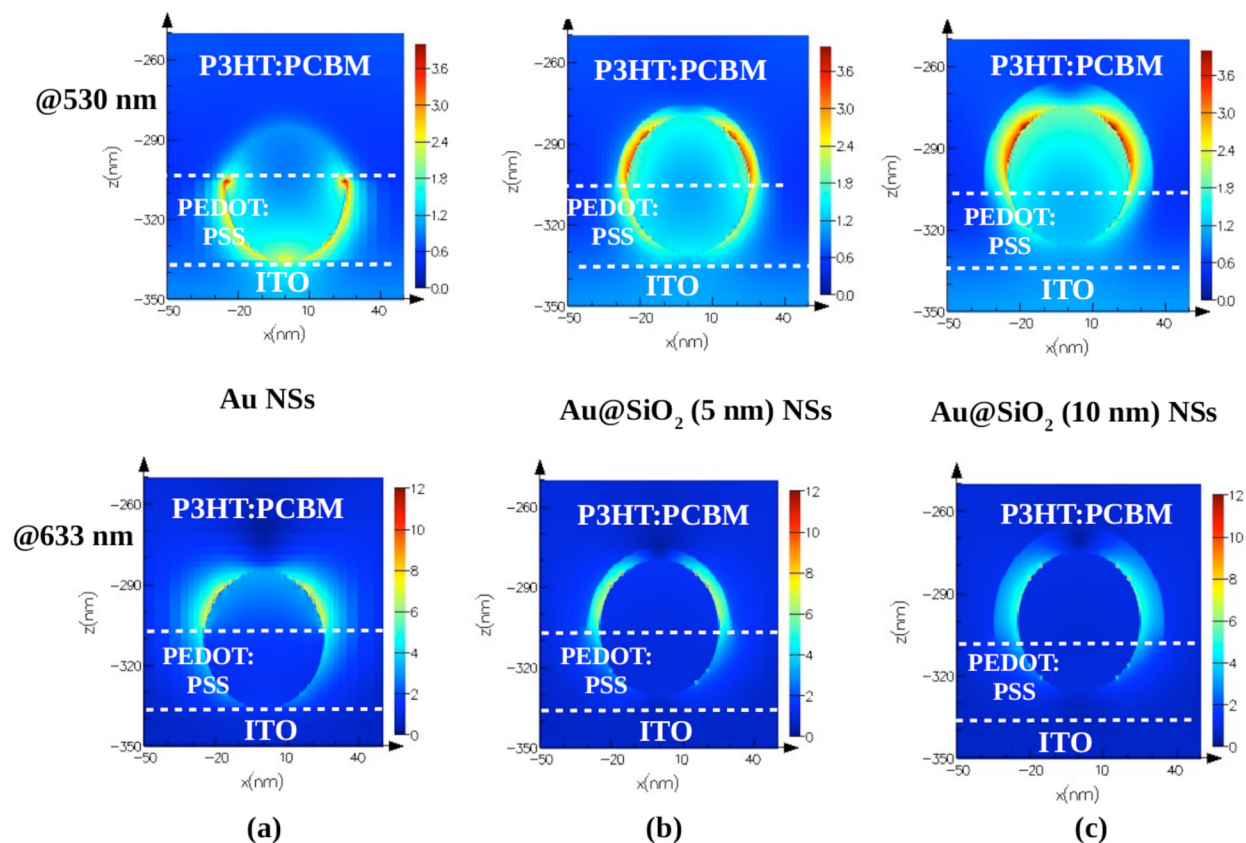


FIG. 4. Electromagnetic field intensity distributions around Au@SiO<sub>2</sub> NSs in OSCs at the wavelengths of 530 nm (top) and 633 nm (bottom) for (a) 0 nm, (b) 5 nm, and (c) 10 nm-thick silica shell.

wavenumber range of 600–1600 cm<sup>-1</sup>. The two most dominant modes from P3HT are observed at 1380 and 1445 cm<sup>-1</sup>, which correspond to the C–C skeletal stretch and the C=C symmetric stretch modes, respectively.<sup>41,42</sup> Another peak at 995 cm<sup>-1</sup> (C–C<sub>alkyl</sub>) and a component of the 1210 cm<sup>-1</sup> complex structure are also attributed to stretching modes identified as (s) in the peak designation of Fig. 5(a). On the other hand, several peaks corresponding to bending and deformation modes are identified as a part of the 1210 cm<sup>-1</sup> band, at 1090 cm<sup>-1</sup> both corresponding to C–H bending vibrational modes and the peaks at 727 and 683 cm<sup>-1</sup>, assigned to the antisymmetric C–S–C ring skeleton in-phase deformation in the thiophene ring of P3HT.<sup>42,43</sup> Moreover, no new peak or any peak position shift is observed in the Raman spectra of samples embedding Au NSs or Au@SiO<sub>2</sub> NSs. In a similar way, Yang *et al.*<sup>44</sup> investigated the plasmonic effects on the molecular order of P3HT:PCBM by using Raman spectroscopy at the excitation wavelength of 633 nm. This wavelength is known to be sensitive to ordered molecules but insensitive to disordered molecules for P3HT of the samples. Their Raman experiments on silver nanowires (Ag NWs) with different sizes integrated in P3HT:PCBM films also revealed that the peak positions of reference and plasmonic samples do not change under 633-nm excitation. The Raman scattering of the plasmonic samples is enhanced compared to that of the reference sample, which would be consistent with the enhancement of the scattering part of absorption spectra.

When comparing the relative intensity of the main peaks at 727 and 1380 cm<sup>-1</sup> with the peak at 1445 cm<sup>-1</sup>, it becomes apparent that the evolution of these peaks within the samples is very different. In Table I, the ratio between both peaks (C–C stretch and C–S–C deformation) and the main peak at 1445 cm<sup>-1</sup> is calculated for each sample. For

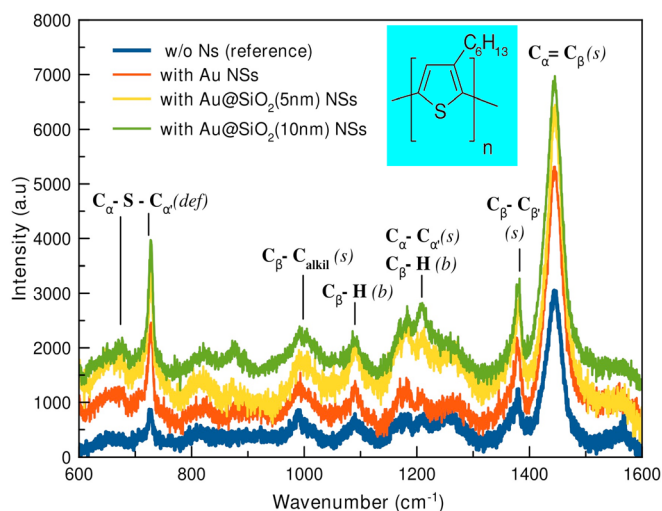


FIG. 5. Raman spectra of reference and Au@SiO<sub>2</sub> plasmonic samples with different silica shell thicknesses under 633 nm wavelength excitation. The baselines of the spectra are shifted vertically for presentation clarity. The inset presents the chemical structures of P3HT.

TABLE I. Relative intensity ratio between the C-S-C deformation mode at  $727\text{ cm}^{-1}$  (top) and the C-C stretching mode at  $1380\text{ cm}^{-1}$  (bottom) with the main peak of the spectra in the  $1445\text{ cm}^{-1}$  C=C stretching mode.

Ratio	W/o NS	With Au NS	With Au@SiO <sub>2</sub> (5 nm) NS	With Au@SiO <sub>2</sub> (10 nm) NS
$I_{\text{C-S-C}}/I_{\text{C=C}}$	0.26	0.36	0.48	0.45
$I_{\text{C-C}}/I_{\text{C=C}}$	0.41	0.31	0.35	0.32

the C-S-C deformation mode, there is an increase in the relative ratio for the plasmonic samples. These augmentations in relative intensity have already been observed when P3HT is subjected to an oxidative doping,<sup>45,46</sup> when a redistribution of charges inside the polymer is achieved to accommodate the doping. Nevertheless, in that case, this increase is also accompanied by an increase in the intensity of the C-C stretching mode at  $1380\text{ cm}^{-1}$ . This is not what it happens in our case, as it is for the reference sample when we find the largest relative intensity for this mode. This difference of behavior can be tentatively explained by the impact of the local electric field created by the plasmonic structures in the C-S-C ring deformations, which will be more important in the case of two different atomic species involved in the vibration mode than in the case of the same atomic species (C-C). The Raman spectroscopy results indicate that the LSPR induced electromagnetic field strength enhancement would not change the Raman peak position but increase its intensity, which is in adequacy with our FDTD simulations and the UV-Vis absorption results as presented above.

#### IV. CONCLUSION

We successfully synthesized Au nanospheres with various silica shell thicknesses (Au@SiO<sub>2</sub> NSs) as presented in the TEM images. The optical behavior of organic bulk heterojunctions is enhanced by embedding Au@SiO<sub>2</sub> NSs with different shell thicknesses within the PEDOT:PSS buffer layer and partly penetrating inside the active layer. Our experiment and theoretical optical absorption results in the visible range highlight a broadband absorption enhancement in the concerned plasmonic samples especially with Au@SiO<sub>2</sub> (5 nm) NSs. This light absorption increase can be mainly attributed to the far-field scattering from the large size Au@SiO<sub>2</sub> NSs and partially to the near-field enhancement effect owing to the LSPR. If a thick shell is employed, the FDTD simulation results confirm that the electromagnetic field is primarily located in the dielectric shell and should not contribute significantly to the absorption in the active layer. The Raman spectroscopy results indicate an enhancement of C-S-C related vibration modes of the P3HT molecule after embedding Au@SiO<sub>2</sub> NSs, which are more intense in the case of the 5 nm SiO<sub>2</sub> shell, due to the presence of the plasmonic near-field effect. Furthermore, no new peaks or peak position shifts are observed in the Raman spectra, which suggests that the main structure of the polymer layer remains unchanged. Finally, we demonstrate that the optical behavior of gold-silica core-shell nanospheres embedded in an organic matrix highly depends on the shell thickness and that the highest optical enhancement is obtained for plasmonic samples including NSs with an optimized shell

thickness of 5 nm. Such absorption phenomena can further be engineered to improve light harvesting of OSC and can pave the way for efficient plasmonic OSCs.

#### ACKNOWLEDGMENTS

The authors acknowledge the IDB Merit Scholarship Programme for High Technology (MSP) for financial support. M.T.D. acknowledges the LABEX project (under the Contract ANR-10-LABX-42) in the framework of IdEx Bordeaux (ANR-10-IDEX-03-02).

- <sup>1</sup>K. Zhang, Z. Hu, C. Sun, Z. Wu, F. Huang, and Y. Cao, *Chem. Mater.* **29**, 141 (2017).
- <sup>2</sup>X. Jia, L. Shen, M. Yao, Y. Liu, W. Yu, W. Guo, and S. Ruan, *ACS Appl. Mater. Interfaces* **7**, 5367–5372 (2015).
- <sup>3</sup>C. B. Nielsen, S. Holliday, H.-Y. Chen, S. J. Cryer, and I. McCulloch, *Acc. Chem. Res.* **48**, 2803 (2015).
- <sup>4</sup>W. Zhao, S. Li, H. Yao, S. Zhang, Y. Zhang, B. Yang, and J. Hou, *J. Am. Chem. Soc.* **139**, 7148–7151 (2017).
- <sup>5</sup>L. Lu, W. Chen, T. Xu, and L. Yu, *Nat. Commun.* **6**, 7327–7334 (2015).
- <sup>6</sup>H.-Y. Park, D. Lim, S.-H. Oh, P.-H. Kang, G. Kwak, and S.-Y. Jang, *Org. Electron.* **15**, 2337–2345 (2014).
- <sup>7</sup>D. Duché, P. Torchio, L. Escoubas, F. Monestier, J.-J. Simon, F. Flory, and G. Mathian, *Sol. Energy Mater. Sol. Cells* **93**, 1377–1382 (2009).
- <sup>8</sup>K. N'Konou and P. Torchio, *J. Nanophotonics* **12**, 012502 (2017).
- <sup>9</sup>D.-H. Ko, J. R. Tumbleston, L. Zhang, S. Williams, J. M. DeSimone, R. Lopez, and E. T. Samulski, *Nano Lett.* **9**, 2742–2746 (2009).
- <sup>10</sup>D. Duché, C. Masclaux, J. Le Rouzo, and C. Gourgon, *J. Appl. Phys.* **117**, 053108 (2015).
- <sup>11</sup>E. S. Arinze, B. Qiu, G. Nyirjesy, and S. M. Thon, *ACS Photonics* **3**, 158–173 (2016).
- <sup>12</sup>S. Vedraïne, P. Torchio, A. Merlen, J. Bagierek, F. Flory, A. Sangar, and L. Escoubas, *Sol. Energy Mater. Sol. Cells* **102**, 31–35 (2012).
- <sup>13</sup>Y. Hao, Y. Hao, Q. Sun, Y. Cui, Z. Li, T. Ji, H. Wang, and F. Zhu, *Mater. Today Energy* **3**, 84–91 (2017).
- <sup>14</sup>J.-Y. Jheng, P.-T. Sah, W.-C. Chang, J.-H. Chen, and L.-H. Chan, *Dyes Pigm.* **138**, 83–89 (2017).
- <sup>15</sup>Z. Wang, Y. Hao, W. Wang, Y. Cui, Q. Sun, T. Ji, Z. Li, H. Wang, and F. Zhu, *Synth. Met.* **220**, 612–620 (2016).
- <sup>16</sup>M. Salvador, B. A. MacLeod, A. Hess, A. P. Kulkarni, K. Munechika, J. I. L. Chen, and D. S. Ginger, *ACS Nano* **6**, 10024–10032 (2012).
- <sup>17</sup>V. Jankovic, Y. M. Yang, J. You, L. Dou, Y. Liu, P. Cheung, J. P. Chang, and Y. Yang, *ACS Nano* **7**, 3815–3822 (2013).
- <sup>18</sup>J. L. Wu, F. C. Chen, Y. S. Hsiao, F. C. Chien, P. Chen, C. H. Kuo, M. H. Huang, and C. S. Hus, *ACS Nano* **5**, 959–967 (2011).
- <sup>19</sup>S. Baek, J. Noh, C. Lee, B. S. Kim, M. Seo, and J. Lee, *Sci. Rep.* **3**, 1726 (2013).
- <sup>20</sup>L. Lu, Z. Luo, T. Xu, and L. Yu, *Nano Lett.* **13**, 59 (2013).
- <sup>21</sup>M. Krassas, G. Kakavelakis, M. M. Stylianakis, N. Vaenas, E. Stratakis, and E. Kymakis, *RSC Adv.* **5**, 71704–71708 (2015).
- <sup>22</sup>H. Choi, J. P. Lee, S. J. Ko, J. W. Jung, H. Park, S. Yoo, O. Park, J. R. Jeong, S. Park, and J. Y. Kim, *Nano Lett.* **13**, 2204–2208 (2013).
- <sup>23</sup>Y. Hao, J. Song, F. Yang, Y. Hao, Q. Sun, J. Guo, Y. Cui, H. Wang, and F. Zhu, *J. Mater. Chem. C* **3**, 1082 (2015).
- <sup>24</sup>R. Zhang, Y. Zhou, L. Peng, X. Li, S. Chen, X. Feng, Y. Guan, and W. Huang, *Sci. Rep.* **6**, 25036 (2016).
- <sup>25</sup>X. Xu, Q. Du, B. Peng, Q. Xiong, L. Hong, H. V. Demir, T. K. S. Wong, A. K. K. Kyaw, and X. Sun, *Appl. Phys. Lett.* **105**, 113306 (2014).
- <sup>26</sup>K. N'Konou, L. Peres, and P. Torchio, *Plasmonics* **13**, 297–303 (2018).
- <sup>27</sup>B. Chen, W. Zhang, X. Zhou, X. Huang, X. Zhao, H. Wang, M. Liu, Y. Lu, and S. Yang, *Nano Energy* **2**, 906–915 (2013).
- <sup>28</sup>K. L. Kelly, E. Coronado, L. L. Zhao, and G. C. Schatz, *J. Phys. Chem. B* **107**, 668–677 (2003).
- <sup>29</sup>C. D'Andrea, B. Fazio, P. G. Gucciardi, M. C. Giordano, C. Martella, D. Chiappe, and A. Toma, *J. Phys. Chem. C* **118**, 8571 (2014).
- <sup>30</sup>J. Gao and J. K. Grey, *J. Chem. Phys.* **139**, 044903 (2013).
- <sup>31</sup>A. Wang, H. P. Ng, Y. Xu, Y. Li, Y. Zheng, J. Yu, F. Han, F. Peng, and L. Fu, *J. Nanomater.* **2014**, 451232.
- <sup>32</sup>J. Rodríguez-Fernández, J. Pérez-Juste, F. Javier García de Abajo, and L. M. Liz-Marzán, *Langmuir* **22**, 7007–7010 (2006).
- <sup>33</sup>N. R. Jana, *Chem. Commun.* **9**, 1950–1951 (2003).

- <sup>34</sup>C. Fernandez-Lopez, C. Mateo-Mateo, R. Alvarez-Puebla, J. Perez-Juste, I. Pastoriza-Santos, and L. M. Liz-Marzan, *Langmuir* **25**, 13894–13899 (2009).
- <sup>35</sup>W. Stöber, A. Fink, and E. Bohn, *J. Colloid Interface Sci.* **26**, 62–69 (1968).
- <sup>36</sup>M.-H. Hsu, P. Yu, J.-H. Huang, C.-H. Chang, C.-W. Wu, Y.-C. Cheng, and C.-W. Chu, *Appl. Phys. Lett.* **98**, 073308 (2011).
- <sup>37</sup>K. R. Catchpole and A. Polman, *Opt. Express* **16**, 21793 (2008).
- <sup>38</sup>K. R. Catchpole and A. Polman, *Appl. Phys. Lett.* **93**, 191113 (2008).
- <sup>39</sup>F. J. Beck, A. Polman, and K. R. Catchpole, *J. Appl. Phys.* **105**, 114310 (2009).
- <sup>40</sup>S. Vedraïne, P. Torchio, D. Duché, F. Flory, J.-J. Simon, J. Le Rouzo, and L. Escoubas, *Sol. Energy Mater. Sol. Cells* **95**, S57–S64 (2011).
- <sup>41</sup>D. E. Motaung, G. F. Malgas, C. J. Arendse, S. E. Mavundla, and D. Knoesen, *Mater. Chem. Phys.* **116**, 279–283 (2009).
- <sup>42</sup>V. Saini, Z. R. Li, S. Bourdo, E. Dervishi, Y. Xu, X. D. Ma, V. P. Kunets, G. J. Salamo, T. Viswanathan, A. R. Biris, D. Saini, and A. S. Biris, *J. Phys. Chem. C* **113**, 8023–8029 (2009).
- <sup>43</sup>M. Baibarac, M. Lapkowski, A. Pron, S. Lefrant, and I. Baltog, *J. Raman Spectrosc.* **29**, 825–832 (1998).
- <sup>44</sup>Y. Yang, L. Sun, J. Ou, Y. He, X. Lin, Z. Yuan, W. Lin, W. Hong, D. Yu, X. Chen, and Z. Qiu, *J. Raman Spectrosc.* **47**, 888–894 (2016).
- <sup>45</sup>M. Trznadel, M. Zagorska, M. Lapkowski, G. Louarn, S. Lefrante, and A. Prona, *J. Chem. Soc., Faraday Trans.* **92**, 1387–1393 (1996).
- <sup>46</sup>M. Stavytska-Barba, M. Salvador, A. Kulkarni, D. S. Ginger, and A. M. Kelley, *J. Phys. Chem. C* **115**, 20788–20794 (2011).